Optimization of a parallel hole collimator/CdZnTe gamma-camera architecture for scintimammography

Charlotte Robert, Guillaume Montémont,[a] Véronique Rebuffel, and Loïck Verger
CEA–LETI–MINATEC, F38054 Grenoble, France

Irène Buvat
IMNC–UMR 8165 CNRS, Universités Paris 7 et 11, Bâtiment 440, 91406 Orsay, France

(Received 3 May 2010; revised 31 January 2011; accepted for publication 6 February 2011; published 9 March 2011)

Purpose: Small field-of-view CdZnTe (CZT) gamma cameras are increasingly studied for breast lesion detection to complement mammography or ultrasonographic findings. However, in classical collimation configurations, they remain limited by the trade-off between spatial resolution and sensitivity. The HiSens architecture was proposed to overcome these limitations. Using an accurate 3D localization of the interactions inside the detector, this architecture leads to a gain in sensitivity without loss in spatial resolution. In this article, the relevance of the HiSens architecture for planar scintimammography is studied.

Methods: A detective quantum efficiency (DQE) computation method is developed and used to optimize the dimensioning of a parallel hole collimator dedicated to scintimammography. Based on the DQE curves, the impact of the collimator-to-detector distance is studied. Two algorithms are proposed to combine data acquired with different collimator-to-detector distances.

Results: It is shown that CZT detector virtual pixelization increases system sensitivity by 3.3 while preserving a standard LEHR spatial resolution. The introduction of a gap between the CZT detector and the collimator is useful to modulate the DQE curve shape. The combination of data acquired using different gaps in the image formation process leads to enhanced restoration of the frequency content of the images, resulting in image contrast and spatial resolution improvements.

Conclusions: Acquisition duration or injected activity could be markedly reduced if the HiSens architecture with an appropriate collimator-detector gap were used. © *2011 American Association of Physicists in Medicine*. [DOI: 10.1118/1.3560423]

Key words: scintimammography, breast imaging, gamma-camera, CZT, collimator optimization, DQE

I. INTRODUCTION

In the United States and Western Europe, breast carcinoma is today the most common cancer in women.[1] Early lesion detection is of foremost importance for successful treatment. Clinical breast exams and mammographies are currently used for screening. However, these techniques have limited sensitivity for in-depth and axillary lesions.[2] In the case of dense breasts, lesion detection rate decreases from a range of 71%–96% (normal breasts)[3] to a range of 48%–63% (dense breasts)[4–6] when only mammography is used. As women with dense breasts have an increased risk of developing breast cancers,[7] additional imaging methods are currently being investigated to improve the breast cancer diagnosis.[8] In this paper, we focus on scintimammography, which has the advantage of being virtually not affected by breast density.

Scintimammography is a functional imaging method that detects the uptake of a radiotracer in the breast with a gamma camera. This technique traditionally uses classical Anger gamma cameras, based on NaI(Tl) detectors, with typical fields of view of 50×50 cm^2. However, these detectors make it difficult to position the breast close to the detector, and the resulting spatial resolution is only about 1 cm.

In the past ten years, dedicated small field-of-view scintillator-based gamma cameras have been designed.[9,10] Two systems, the 6800 system (Dilon Diagnostics®, Newport News, VA) and the 2020tc Imager (Digirad, San Diego, CA), respectively, based on NaI(Tl) and CsI(Tl) crystals, are now on the market. Their small size makes it possible to reduce the breast-detector distance. Based on a pixelated architecture, these systems improve the spatial resolution and the visualization of subcentimetric lesions compared to conventional gamma cameras.[10–12] Compared to mammography, sonography, and MRI systems, it was shown that these small field-of-view dedicated gamma cameras have excellent sensitivities for the breast cancer detection.[13–15]

More recently, several laboratories have developed and assessed pixelated CdZnTe (CZT) small field-of-view gamma imagers.[16–19] A system based on this technology, the LumaGem 3200s system (Gamma-Medica Inc., Northridge, CA), is commercially available.[20] Several reasons motivated this transition to the CZT semiconductor material. First, CZT detectors offer a high intrinsic spatial resolution, equal to the electrode size. This feature is of great importance for the detection of subcentimetric lesions placed close to the collimator face.[12] Moreover, as they do not require the use of photomultiplier tubes (PMTs) and the associated electronic

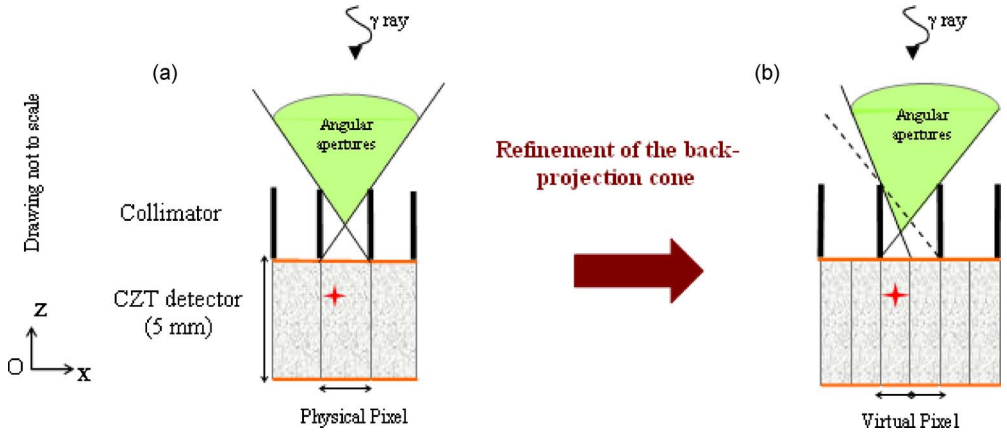

FIG. 1. Angular collimator apertures associated with (a) 1 pixel or (b) 4 virtual pixels per collimator hole.

board is only a few centimeters thick, they are more compact than a NaI(Tl) crystal associated with PMTs, which facilitates compactness and close proximity imaging. Finally, CZT detectors offer a better energy resolution (~3% FWHM at 140 keV) than NaI(Tl) crystals (~9% FWHM at 140 keV).[21] However, this enhanced energy resolution has only a limited impact on scintimammography, according to Hruska and O'Connor,[12] due to the relatively low scatter in breast imaging. Encouraging results have already been obtained with the CZT-based systems, such as high sensitivity (~86%) for the detection of small breast lesions (<1 cm).[17] However, these systems are still associated with high resolution collimators, which greatly limit potential detection efficiency. As a result, the effective dose per scan, which is about 6.7 mSv,[22] cannot be significantly decreased by using CZT detectors only.

To further improve the performance of gamma cameras, our laboratory has proposed an innovative architecture known as HiSens.[23] This architecture is based on pixelated CZT detectors,[24] like the CZT prototypes mentioned above, and is also characterized by a large aperture collimator to improve system sensitivity. Moreover, a dedicated electronics accurately locates photon-detector interactions[25] by retrieving the depth-of-interaction (DOI) information and by using a CZT detector sampling less than the electrode size. Such accurate positioning of the detected photons yields a high spatial resolution despite the use of a high sensitivity collimator. The HiSens geometry and associated reconstruction algorithms have been previously validated in planar and SPECT modes using simulations and experiments.[26]

In the present paper, the relevance of the HiSens architecture is studied in the context of planar scintimammography. This application, for which the detection of small lesions is of great interest (<1 cm in diameter,[17,18] corresponding to spatial frequencies >1 cm^{-1}), is appealing for the HiSens architecture, which significantly improves the restoration of high spatial frequencies.[26] The aim of the study is to optimize the collimator parameters and to evaluate the maximum sensitivity gain achievable using HiSens without loss in spatial resolution compared to low-energy high resolution (LEHR) systems. For that purpose, a DQE computation method is developed. Based on the DQE curves, the role of a new parameter, the collimator-to-detector distance, is studied, and the value for this parameter is optimized in addition to the collimator dimensions. Two algorithms are proposed to combine data acquired for different collimator-to-detector distances. All results are validated using Monte Carlo simulations. An experimental validation is also presented to validate part of the results.

II. BACKGROUND: HISENS ARCHITECTURE DESCRIPTION

The HiSens architecture consists of a pixelated CZT detector, a dedicated electronics for 3D localization, a parallel-square hole collimator, and an algorithm to estimate the planar image from the acquired data. A large aperture collimator is used to increase system sensitivity. To maintain a correct spatial resolution despite the large aperture collimator, a collimator response deconvolution is performed even in the planar acquisition mode. This deconvolution is feasible, thanks to the accurate 3D positioning of the photon interactions inside the CZT detector obtained using biparametric spectra[21,24] and barycentric calculation.[25,27–29] Barycentric calculation, which uses the signal of the adjacent anodes to locate the x and y positions inside the physical detector pixel (electrode), does not increase the number of read-out channels. Figures 1 and 2 illustrate how the resampling (fine pixelization of the CZT detector and DOI information) reduces the backprojection cones compared to a conventional architecture. This resampling is referred to as HiSens processing hereafter in this paper.

III. MATERIAL AND METHODS

III.A. Simulated HiSens architecture

In scintimammography, preference is given to small field-of-view gamma cameras to place the breast in close proximity to the detector. In our study, a 224×224 mm CZT detector was considered. Its thickness was set to 5 mm in order to obtain the detection sensitivity of a conventional NaI(Tl) Anger camera (85% at 140 keV). To study the impact of detector spatial sampling (Fig. 1), four virtual detector pixel

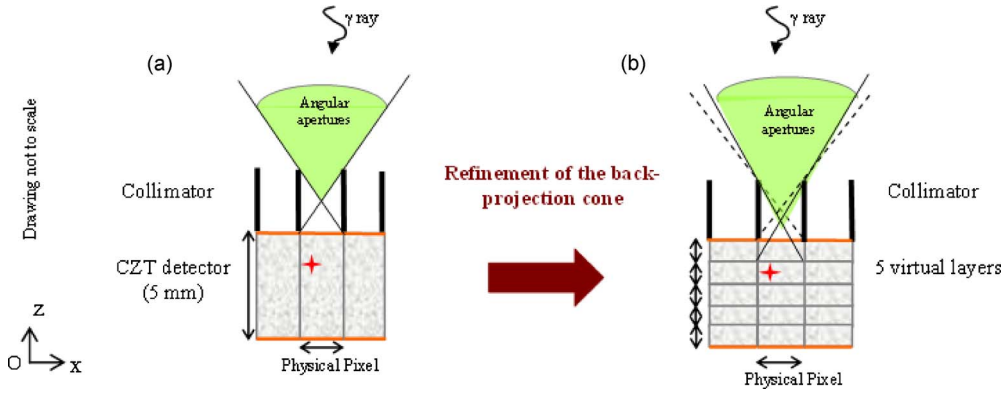

FIG. 2. Different angular collimator apertures associated with (a) one layer of 5 mm or (b) five layers of 1 mm of CZT detector.

sizes were considered: 1.6, 0.8, 0.4, and 0.2 mm, which corresponded to 1, 4, 16, and 64 virtual pixels per collimator hole, respectively. The detector was also divided into three equally sensitive virtual layers (the thickness of each layer was set in such a way that layers detected equal numbers of photons) to take advantage of the DOI information. Finally, a configuration with only one 5 mm thick CZT detector layer was studied as a reference.

In conventional gamma-camera architectures, the detector is next to the collimator to avoid multiplexing: A detector pixel can be reached only by photons entering through a given collimator hole (Fig. 3)—assuming no septal penetration. In this work, we study the impact of increasing collimator-to-detector distance, c, on system's performance. Collimator-to-detector distances ranging from 1 to 10 mm were investigated. The 1 mm collimator-to-detector distance was considered as the reference value used in conventional systems.

III.B. DQE calculation and collimator optimization

To optimize the tungsten parallel hole collimator dimensions for scintimammography when using the HiSens architecture, a DQE calculation approach was used. The DQE is a figure of merit characterizing the effective sensitivity for each spatial frequency, where the spatial frequency refers to the inverse of the periodicity with which the image intensity value changes. The DQE describes the specific response of a system to a given object. It is useful for comparing detection systems including gamma cameras.[30] The DQE calculation method for gamma imaging is detailed in Ref. 26. It includes several approximations such as the stationary noise hypothesis. This assumption is essential for characterizing the imaging system regardless of the object of investigation. Moreover, the noise is considered as to be only due to the gamma detection statistics, which is valid for photon counting detectors. These assumptions lead to Eq. (1), which gives the DQE expression for the HiSens configuration, in which n {subpixel+virtual layer} sets are considered,

$$\mathrm{DQE} = \sum_{i=0}^{i=n-1} \mathrm{DQE}_i = \sum_{i=0}^{i=n-1} S_i \times \mathrm{MTF}_i^2. \quad (1)$$

In Eq. (1), S_i and MTF_i are the sensitivity and the modulation transfer function (MTF) corresponding to {subpixel+virtual layer} set i. Figure 4 illustrates the DQE calculation method.

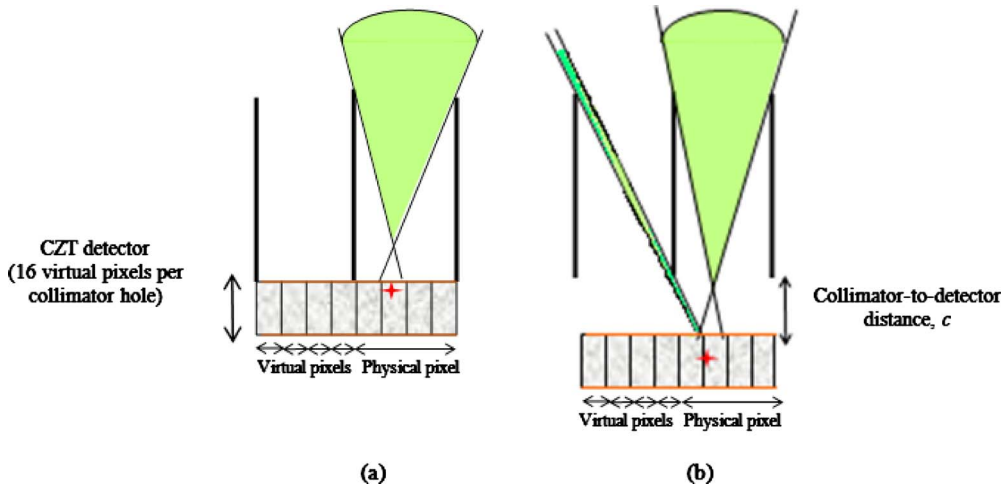

FIG. 3. Illustration of multiplexing. (a) $c=0$ mm—No multiplexing. (b) $c\neq 0$ mm—Multiplexing: Photons arriving from different collimator holes can hit the same detector pixel.

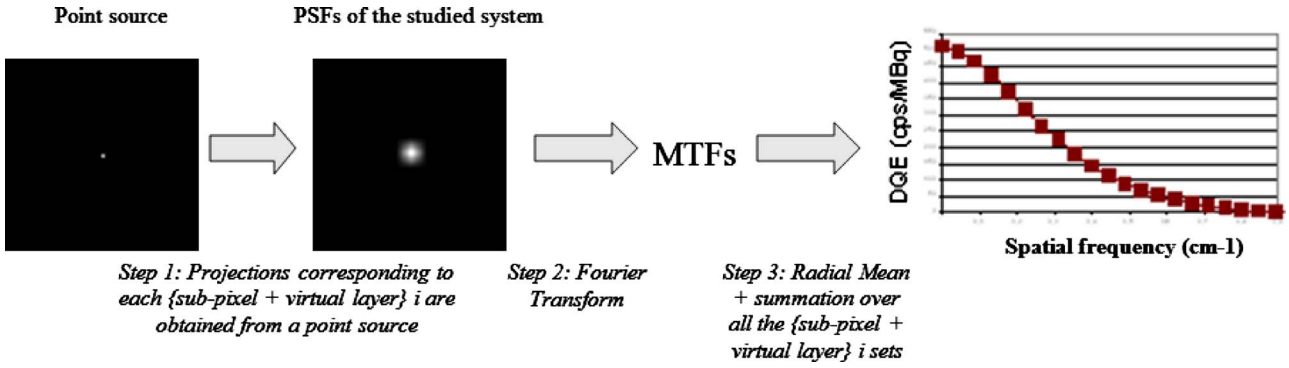

FIG. 4. Implementation of the DQE value calculation.

First, the point spread function (PSF) corresponding to each {subpixel+virtual layer} set is obtained from a point source. A Fourier transform is then applied to each PSF to obtain the corresponding MTF. Performing a radial mean and a summation over all sets finally yields the DQE curve, which describes the system response as a function of the spatial frequency.

To optimize the collimator parameters, PSFs and MTFs were calculated for each collimation configuration. As ^{99} ^{m}Tc is the relevant isotope for scintimammography, the analytical simulation software SINDBAD (Ref. 31) was used to obtain projections of ^{99} ^{m}Tc (140 keV) point sources [Fig. 5(a)].

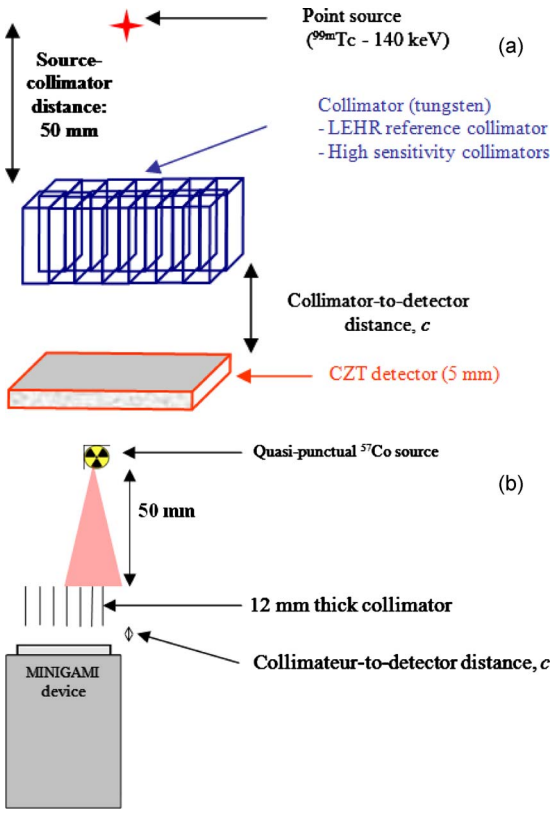

FIG. 5. (a) Simulated configuration for the DQE calculation. (b) Experimental setup used for the experimental DQE calculation.

Scintimammography protocols recommend the use of high resolution collimators.[32] For this reason, a LEHR collimator was first simulated (1.6 mm pitch, 0.15 mm septal thickness, 29 mm septal height, resulting in a 10^{-4} efficiency). The LEHR performances were compared to those of the collimators associated with the HiSens architecture.

We first studied the impact of the fine CZT detector over-pixelization on the DQE values. An arbitrary low-energy high sensitivity (LEHS) collimator was considered. Except for its height (16 mm), its characteristics were the same as those of the LEHR collimator. A gap between the collimator and the detector was introduced. The gap thickness c was set to 1, 5, and 10 mm.

Several high sensitivity collimators were then investigated. They all had the same pitch, $p=1.6$ mm, but their heights varied from 8 to 22 mm. The septal thicknesses were set in such a way that the septal penetration, s, was smaller than 5% [Eq. (2)].

$$s \geq -\left(\frac{2p\,\ln(\beta)/\mu}{a+\ln(\beta)/\mu}\right)\times\left(\frac{a\mu+\ln(\beta)}{a\mu-\ln(\beta)}\right), \tag{2}$$

where a is the collimator height, μ is the tungsten linear attenuation coefficient (3.6 mm^{-1} at 140 keV), and β depends on the desired septal penetration value (0.05 in our case). Table I summarizes the parameters of the simulated collimators. Finally, the collimator-to-detector distance c varied from 1 to 10 mm for each high sensitivity collimator.

To reproduce a scintimammography scan, the DQE values were calculated for a point source located 50 mm from the collimator surface. This 50 mm distance, which corresponds to the mean thickness of a breast, is frequently used to optimize breast imaging systems.[33] This assumes that the breast is in contact with the collimator surface and that only one detector head is used. This distance can be halved if a dual-head system is used.[16]

The DQE curves were plotted for each configuration described above (8–22 mm collimator thickness, 1–10 mm collimator-to-detector distance, 1–64 virtual pixels per collimator hole, without and with DOI information). All DQE curves were compared to the curve corresponding to the reference LEHR collimator for equivalent acquisition durations.

TABLE I. Features (septal height, pitch, hole width, septal thickness, and total sensitivity) of the reference LEHR collimator and of the 15 simulated high sensitivity collimators.

Collimator	Septal height (mm)	Pitch (mm)	Hole width (mm)	Septal thickness (mm)	Calculated total sensitivity (counts/MBq)
LEHR	29	1.6	1.45	0.15	105
LEHS	16	1.6	1.45	0.15	355
H08	8	1.6	1.30	0.300	986
H09	9	1.6	1.33	0.270	841
H10	10	1.6	1.35	0.250	714
H11	11	1.6	1.375	0.225	628
H12	12	1.6	1.39	0.210	546
H13	13	1.6	1.40	0.200	475
H14	14	1.6	1.42	0.180	431
H15	15	1.6	1.43	0.170	384
H16	16	1.6	1.44	0.160	346
H17	17	1.6	1.45	0.150	313
H18	18	1.6	1.45	0.150	278
H19	19	1.6	1.465	0.135	260
H20	20	1.6	1.47	0.130	237
H21	21	1.6	1.475	0.125	217
H22	22	1.6	1.48	0.120	200

Lesions of interest in scintimammography should be detected as soon as possible. We therefore chose to perform DQE measurements for spatial frequencies ranging from 0 to 3 cm^{-1}, corresponding to lesions at least 3.3 mm in diameter (smaller sizes would be out of reach for the considered detector given the 1.6 mm collimator hole).

III.C. Assessment of image quality

To validate the DQE-based optimization and assess the detection system spatial resolution, projections of a Derenzo phantom [Fig. 6(a)] including rods between 8 and 1.6 mm in diameter, i.e., rods with diameters of clinical interest, were simulated using the GATE Monte Carlo simulation tool.[34] The phantom (73.6 mm × 73.6 mm × 38.4 mm) included $^{99\,m}$Tc (140 keV) and had a voxel size of 0.8 × 0.8 × 0.8 mm^3. The rod-to-background activity ratio was set to 6.[35] For each collimation configuration, the source-to-collimator distance was set to 50 mm [Fig. 6(b)], and the acquisition duration was adjusted to obtain 1 Mcount/projection. All physical effects (i.e., photoelectric, Compton, and Rayleigh) were modeled in the GATE simulations. An almost ideal detector was simulated: Only a limited energy resolution of 4% at 140 keV was modeled using a Gaussian energy blur, but no spatial blurring was included. The low tail seen in CZT detectors[20] was not modeled as we subsequently considered only events detected in the narrow 133–147 keV energy window.

An ordered subset expectation maximization (OSEM) algorithm dedicated to the HiSens architecture was previously developed.[23] It was used to reconstruct the image from the detected signal, even in the planar acquisition mode. The system matrix was analytically calculated using SINDBAD. As the convergence speed of the algorithm depends on the collimation configuration, the high-frequency noise [Eq. (3)] was estimated considering the lukewarm uniform areas of the Derenzo reconstructed images using

$$\text{HF noise} = \frac{1}{N} \sum_{i \in \text{uniform area}} \frac{(\nu_i - m_i)^2}{m_i^2}, \tag{3}$$

where ν_i represents the value of pixel i, m_i is the mean value of the eight adjacent pixels, and N is the pixel number in the uniform area of interest. Based on this noise measurement, the reconstructed images corresponding to the same level of noise could be compared. The contrast of the three largest rods was measured using

$$C = \frac{(\nu_1 - \nu_2)}{(\nu_1 + \nu_2)} \times 100, \tag{4}$$

where ν_1 and ν_2 are the mean pixel values in three areas of 3 × 3 pixels placed in the hot (three largest rods, regions away from the rod edges) and lukewarm regions, respectively.

III.D. Combination of projections acquired for different collimator-to-detector distances

The introduction of the collimator-to-detector distance, c, can yield several projections for a given collimator, one for each c distance. These images can be reconstructed independently with an OSEM algorithm. They can also be combined to obtain a single reconstructed image from the set of projections corresponding to different c values and thus take advantage of the specific restoration of spatial frequencies offered by each c value. Two methods were investigated to combine the acquired projections during the image formation process.

III.D.1. Classical OSEM algorithm

The simplest method for combining the projections consists of using OSEM, with the projections corresponding to the different collimator-to-detector distances, and a system matrix obtained from the juxtaposition of the system matrices corresponding to the different c values. Equation (5) illustrates the inverse problem to be solved when N projections are acquired,

$$\begin{pmatrix} p_{1-1} \\ p_{1-2} \\ \cdots \\ p_{1-K} \\ p_{2-1} \\ p_{2-2} \\ \cdots \\ p_{2-K} \\ \cdots \\ p_{N-1} \\ \cdots \\ p_{N-K} \end{pmatrix} = \begin{pmatrix} r_{1-1-1} & r_{1-1-2} & \cdots & r_{1-1-I} \\ r_{1-2-1} & \cdots & \cdots & r_{1-2-I} \\ \cdots & \cdots & \cdots & \cdots \\ r_{1-K-1} & \cdots & \cdots & r_{1-K-I} \\ r_{2-1-1} & r_{2-1-2} & \cdots & r_{2-1-I} \\ r_{2-2-1} & \cdots & \cdots & r_{2-2-1} \\ \cdots & \cdots & \cdots & \cdots \\ r_{2-K-1} & \cdots & \cdots & r_{2-K-I} \\ \cdots & \cdots & \cdots & \cdots \\ r_{N-1-1} & r_{N-1-2} & \cdots & r_{N-1-I} \\ \cdots & \cdots & \cdots & \cdots \\ r_{N-K-1} & r_{N-K-2} & \cdots & r_{N-K-I} \end{pmatrix} \times \begin{pmatrix} f_1 \\ f_2 \\ \cdots \\ \cdots \\ f_I \end{pmatrix}. \quad (5)$$

In Eq. (5), p_{n-k} is the measurement in detection bin k for the nth acquisition (the nth collimator-to-detector distance), r_{n-k-i} is the probability that a photon emitted in voxel i be detected in detection bin k for the nth collimator-to-detector distance, and f_i is the source activity in voxel i.

The resulting image combining three collimator-to-detector distances (1, 5, and 10 mm) was compared to the three images obtained independently with OSEM considering each collimator-to-detector distance. For this comparison, only one-third of the counts recorded in each of the projections acquired for the thee different c distances was used so that the number of counts in the final image was identical to that in each image obtained from a single c distance.

III.D.2. Wavelet decomposition

The second approach to combine images corresponding to different c values was based on wavelet decomposition.[36] The wavelet representation decomposes an original signal on a wavelet orthogonal basis and can be viewed as a multiresolution tool. It is possible to reconstruct a signal from its wavelet series decomposition using the inverse wavelet transform.[36] The following paragraph explains how the wavelet decomposition and recomposition were implemented

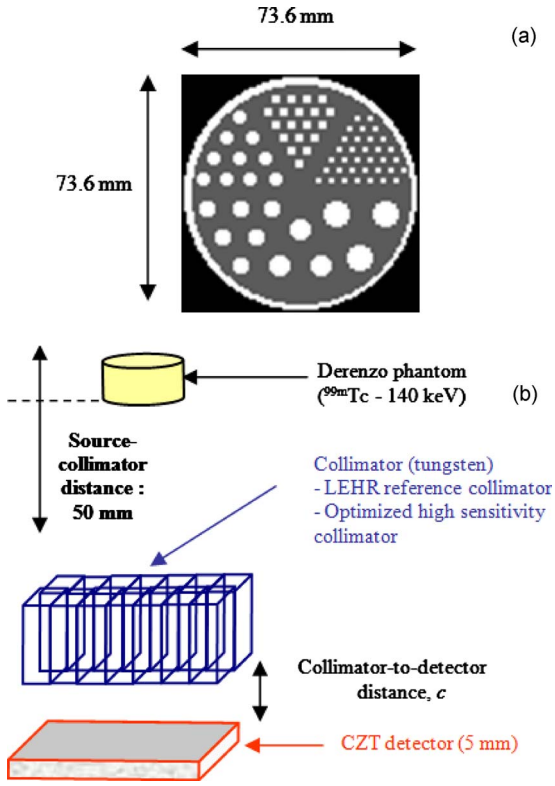

FIG. 6. (a) Cylindrical Derenzo phantom including hot rods of increasing sizes (1.6, 2.4, 4.0, 4.8, 6.4, and 8 mm in diameter). The hot-to-background activity ratio was set to 6:1. (b) Simulated setup involving the Derenzo phantom.

to combine projections acquired with different c values. Unlike in the previous OSEM-based approach, projections were independently reconstructed for each collimator-to-detector distance and were combined afterward.

Let Image_c_n be the reconstructed image corresponding to the nth distance between the collimator and the detector. The combination method works as follows (Fig. 7):

(1) Independent reconstruction of each Image_c_n using conventional OSEM.
(2) Wavelet decomposition of each Image_c_n. The Mallat and Zhong[37] basis was used with a $j=2$ approximation level corresponding to the level of details required in the final low-resolution image. Seven images were obtained for each Image_c_n, as illustrated in Fig. 8: A low-resolution image (LR2 image) and six high resolution images (HR_X2, HR_Y2, HR_X1, HR_Y1, HR_X0, and HR_Y0 images).
(3) Comparison of the entire set of LR2 images (Fig. 8). A final LR2 image is deduced by retaining, for each pixel, the maximum absolute value in that pixel in the set of LR2 images.
(4) The same as step (3) for the HR_Xj and HR_Yj images corresponding to each decomposition level, j.
(5) Wavelet inverse transform from the final LR2, HR_X2, HR_Y2, HR_X1, HR_Y1, HR_X0, and HR_Y0 images.

The recomposed image based on the wavelet decomposi-

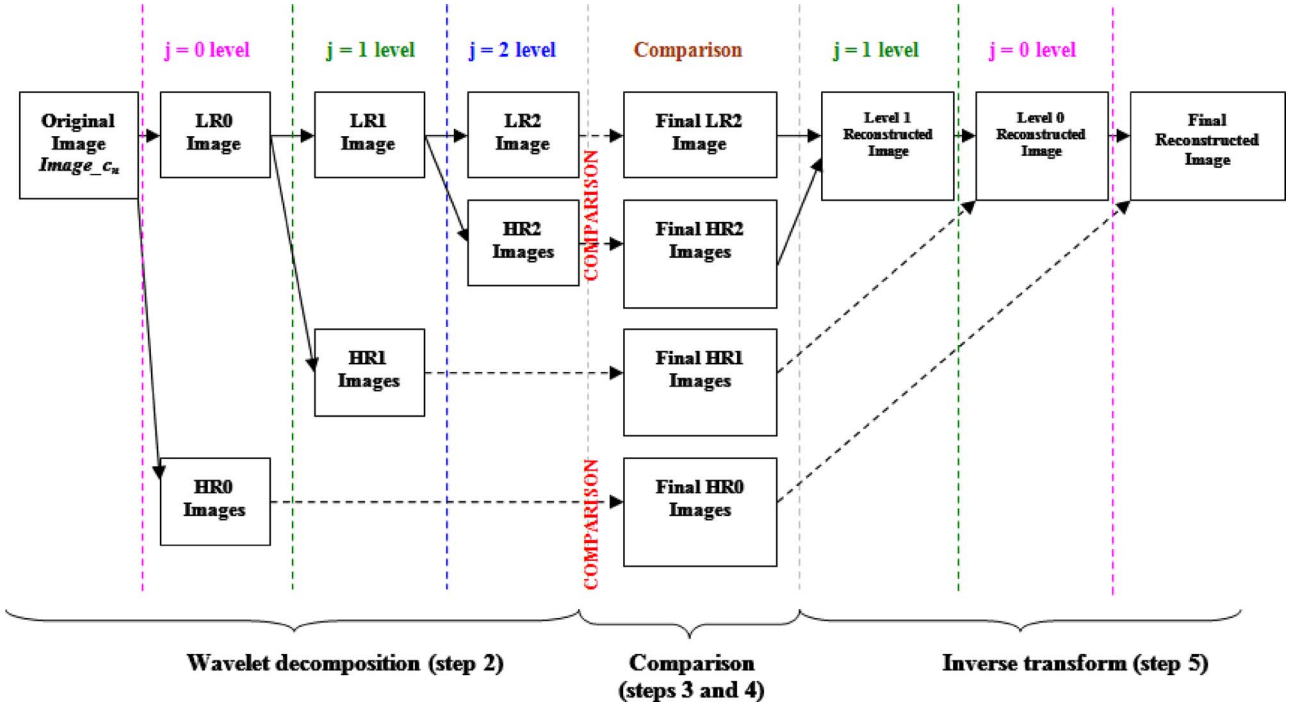

FIG. 7. The use of the wavelet decomposition and recomposition to combine images obtained with different collimator-detector c distances (see text).

tion was compared to the three images corresponding to the 1, 5, and 10 mm collimator-to-detector distances. Again, for this comparison, only one-third of the counts recorded in each of the projections acquired for the three different c distances was used for a fair comparison with the images reconstructed from a single c distance.

III.E. Experimental study

Projections of a ^{57}Co point source (1 mm diameter–185 kBq) placed 50 mm from the collimator plane were acquired [Fig. 5(b)] using a small field-of-view CZT gamma imager.[25] The camera was mechanically translated to acquire all the projections. The detector was 5 mm thick and had 4×4 physical pixels (1.6 mm pixel size). Using the barycentric calculation, each physical pixel was divided into 20×20 virtual pixels (0.08 mm pixel size). A single 5 mm virtual layer was considered. A high sensitivity square hole parallel collimator (H12) was placed in front of the detector. The collimator had 6×6 holes, a 1.6 mm pitch, a 0.15 mm septal thickness, and was 12 mm high. Three collimator-to-detector distances were studied: $c=3$, 5, and 7 mm. Due to an aluminum entrance window, the $c=0$ mm acquisition was not possible. For each collimator-to-detector distance and translation table position, a 1600 s acquisition was performed. No energy window was used.

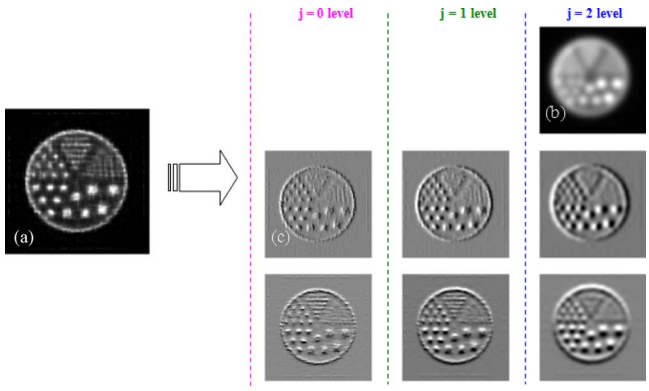

FIG. 8. Illustration of the wavelet decomposition process [step (2) described in the text]: (b) A low resolution image LR2 and (c) six high resolution images (two for each approximation level) were deduced from (a) an initial reconstructed image (Image_c_n).

IV. RESULTS

IV.A. DQE analysis

The arbitrary LEHS (H16) collimator was first considered to study the impact of CZT detector sampling and of collimator-to-detector distance on the DQE curves.

IV.A.1. Impact of detector pixelization on the DQE curves

Figure 9 shows the DQE values obtained with the LEHS collimator for four virtual pixel sizes (1.6, 0.8, 0.4, and 0.2 mm). The DQE curve corresponding to the LEHR collimator (dashed line) was plotted as a reference. In all cases, the collimator-to-detector distance was set to 1 mm.

Considering the DQE values at the 0 cm^{-1} frequency, the sensitivity gain achieved by the reduction in collimator height was roughly 3.6. Moreover, DQE values for the 16 mm thick collimator (green curve) are lower than DQE values for the LEHR collimator for frequencies above 0.9 cm^{-1} when the detector pixel size is set to 1.6 mm (i.e., without

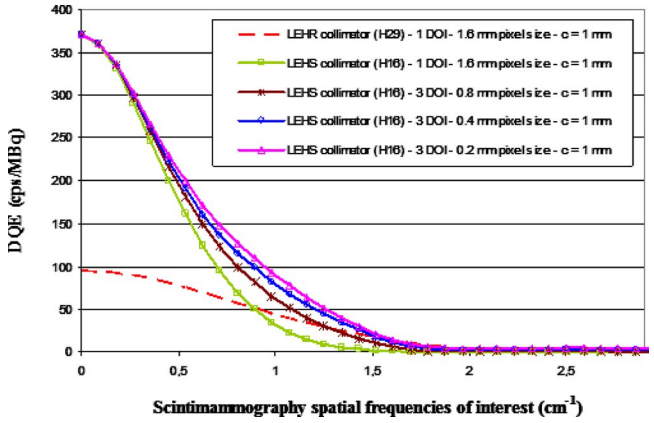

FIG. 9. DQE measured for a 50 mm source-to-collimator distance for two collimation settings (septal heights of 29 and 16 mm). For the LEHR collimator, pixel size was set to 1.6 mm. For the LEHS, four virtual pixel sizes were studied: 1.6, 0.8, 0.4, and 0.2 mm.

HiSens processing). As expected, restoration of high spatial frequencies is markedly reduced if only a large aperture collimator is used. Spatial resampling of the CZT detector (0.8, 0.4, and 0.2 mm virtual pixels) increases the DQE values (Fig. 9). Virtual pixel size was therefore set to 0.2 mm (64 virtual pixels per collimator hole) in the remainder of this study.

IV.A.2. Impact of collimator-to-detector distance on the DQE curves

Figure 10 shows the DQE values obtained with the LEHS collimator when the collimator-to-detector distance was set to 1 and 10 mm, without HiSens processing (1 DOI—1.6 mm pixel size). DQE values corresponding to $c=10$ mm are lower than DQE values obtained for $c=1$ mm. This explains why no gap between the collimator and the detector has been introduced in the gamma camera up to now.

Figure 11 shows the DQE curves corresponding to the LEHS collimator when HiSens processing was used (3 DOI–0.2 mm virtual pixel size), and a gap between the collimator and the detector was introduced ($c=1$, 5, and 10 mm). The DQE curve corresponding to the LEHR collimator is plotted as a reference. The shape of the DQE curves is modulated depending on collimator-to-detector distance. Considering the LEHS–$c=10$ mm configuration, the gap between the collimator and the detector decreases the low-frequency DQE values and increases the high-frequency DQE values compared to smaller gaps. Moreover, comparing the LEHS–$c=5$ mm and the LEHR DQE curves, the 5 mm collimator-to-detector distance yields greater DQE values for all frequencies of interest.

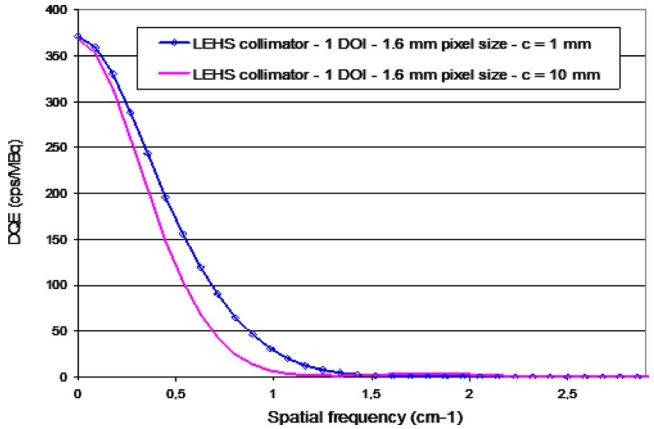

FIG. 10. DQE measured for a 50 mm source-to-collimator distance with the LEHS (H16) collimator for two collimator-to-detector distances: $c=1$ mm and $c=10$ mm, without HiSens processing.

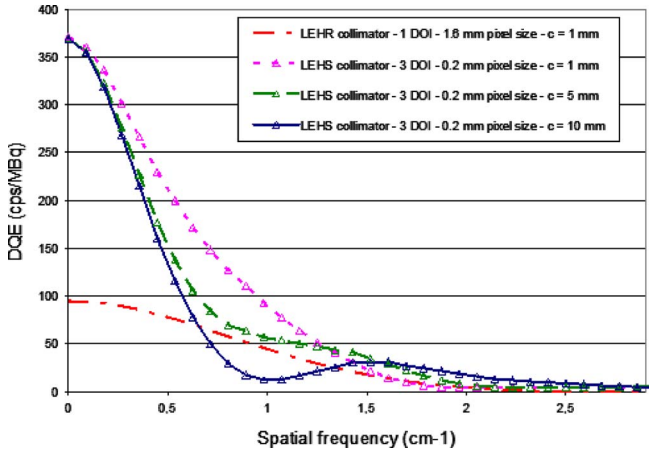

FIG. 11. DQE measured for a 50 mm source-to-collimator distance with the LEHR (H29) and the LEHS (H16) collimators. For the LEHR collimator, no HiSens processing was used and $c=1$ mm. For the LEHS collimator, HiSens processing was used (3 DOI–0.2 mm virtual pixel size) and three collimator-to-detector distances ($c=1$, 5, and 10 mm) were studied.

IV.B. Collimator optimization

Figure 12 compares the DQE curves corresponding to several collimation configurations for a source-to-collimator

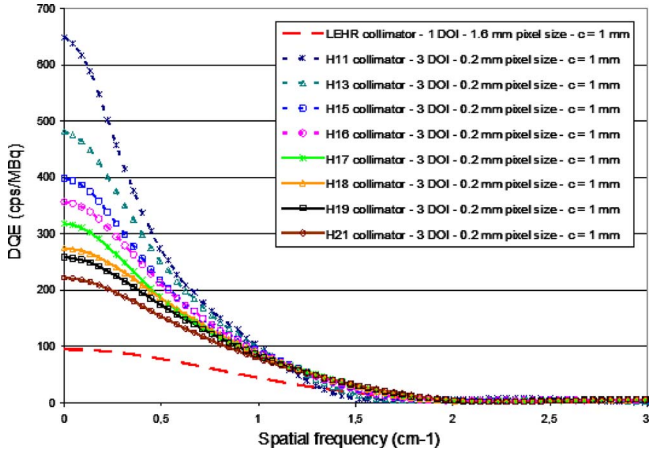

FIG. 12. DQE measured for a source-to-collimator distance of 50 mm with the LEHR (H29) and the high sensitivity collimators. For the LEHR collimator, no HiSens processing was used. For the high sensitivity collimators, HiSens processing was used (3 DOI–0.2 mm virtual pixel size). c was set to 1 mm in all configurations.

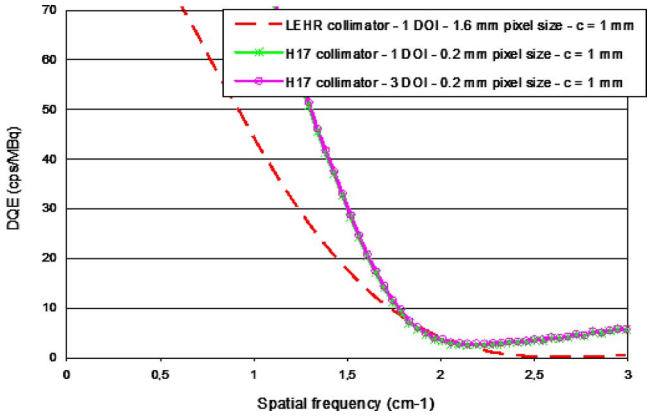

FIG. 13. Zoom on the DQE values measured for a 50 mm source-to-collimator distance with the LEHR (H29) and the high sensitivity H17 collimator. For the LEHR collimator, no HiSens processing was used. For the H17 collimator, HiSens processing was used (1 or 3 DOI–0.2 mm virtual pixel size). c was set to 1 mm in the three configurations.

distance of 50 mm and a collimator-to-detector distance of 1 mm when HiSens processing is used. The LEHR collimator curve is plotted as a reference.

A desirable collimator should recover or improve the high-frequency content (measurable, thanks to the DQE values) captured by the reference LEHR collimator [Eq. (6)] with a maximum sensitivity gain [Eq. (7)]. Comparing all curves plotted in Fig. 12, the H17 collimator fulfills these criteria (Fig. 13). A 3.3 increase in detection sensitivity can therefore be achieved while maintaining the spatial resolution of the LEHR collimator,

$$\mathrm{DQE}_{\mathrm{Optimized\_collimator}}(\nu) \geq \mathrm{DQE}_{\mathrm{LEHR\_collimator}}(\nu), \quad \forall\, \nu \in \text{range of interest}, \tag{6}$$

$$\mathrm{DQE}_{\mathrm{Optimized\_collimator}}(0) \geq \mathrm{DQE}_{\mathrm{Collimator}}(0), \quad \forall\, \text{Collimator}. \tag{7}$$

To further optimize the collimator parameters, the collimator-to-detector distance was made to vary in addition to the collimator septal height. Figure 14 illustrates the DQE ratios (collimator DQE divided by LEHR DQE) obtained for three relevant collimation configurations (H15, H16, and H17). For all these configurations, the DQE ratio was greater than 1 in the frequency range of interest.

According to our criterion [Eq. (6)], the optimized collimator should lead to a DQE ratio greater than 1, i.e., its DQE values should be greater than the reference LEHR DQE values, whatever the frequency. The H17 collimator associated with HiSens and a 5 mm collimator-to-detector distance meets these requirements (Fig. 15). Compared to the $c = 1$ mm configuration, high frequencies are better restored, a fact that is essential for detecting smaller lesions in scintimammography.[17–19]

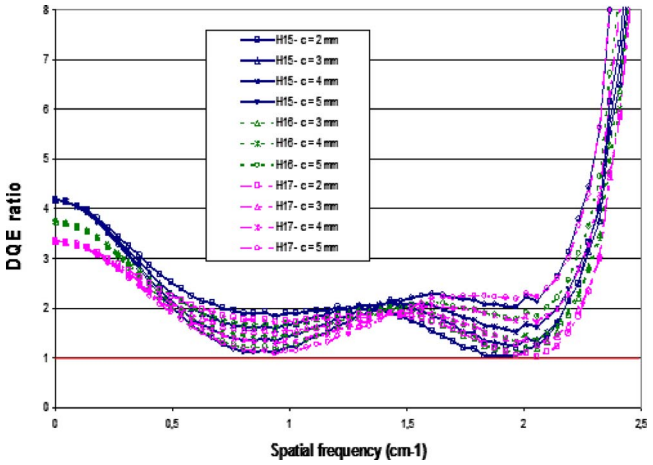

FIG. 14. DQE ratios (collimator DQE divided by LEHR DQE) calculated for relevant high sensitivity collimation configurations.

IV.C. Reconstructed images

Given that the DOI contribution was found to be modest in our geometric conditions (Fig. 13), only one 5 mm layer was considered for the results presented in this subsection.

IV.C.1. Derenzo reconstructed images for a single collimator-to-detector distance

Figure 16 shows the GATE projections of the Derenzo phantom obtained with the LEHR and the optimized H17 HiSens collimators for different collimator-to-detector distances. HiSens processing was applied to the H17 projections (1 DOI–1120 × 1120 pixels–0.2 mm pixel size), but not to the LEHR projection (1 DOI–140 × 140 pixels–1.6 mm pixel size). The five projections have the same count numbers (1 Mcount), which results in an acquisition duration 3.3 times shorter for the H17 HiSens collimator compared to the LEHR collimator. The scatter fraction detected in the 133–147 keV energy window is equal to 14.8% and 16.9% for the LEHR and H17 collimators, respectively. The image deterioration due to the use of a large aperture collimator is clearly visible. A comparison of

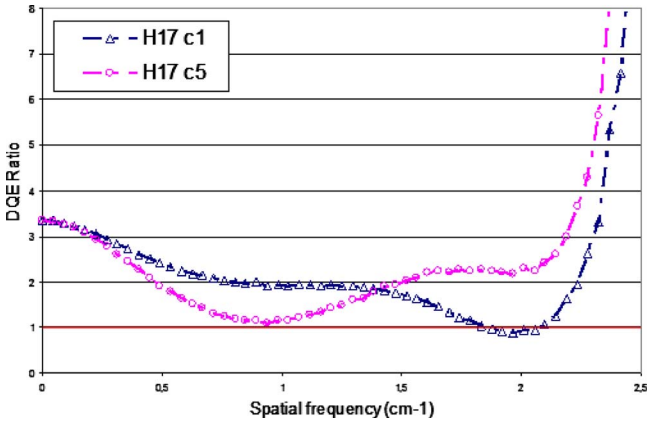

FIG. 15. DQE ratios (collimator DQE divided by LEHR DQE) corresponding to the H17 high sensitivity collimation configuration ($c = 1$ and 5 mm).

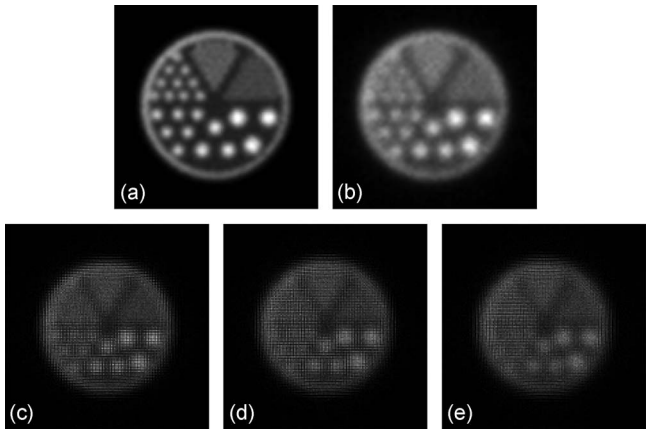

FIG. 16. GATE projections of the Derenzo phantom acquired with (a) the LEHR collimator–1.6 mm detector pixel size–$c=1$ mm, (b) the H17 collimator–1.6 mm detector pixel size–$c=1$ mm, (c) the H17 collimator–0.2 mm detector pixel size–$c=1$ mm, (d) the H17 collimator–0.2 mm detector pixel size–$c=5$ mm, and (e) the H17 collimator–0.2 mm detector pixel size–$c=10$ mm.

Figs. 16(c)–16(e) illustrates the multiplexing phenomenon: The gap between the collimator and the detector leads to blurred images.

Figure 17 compares the reconstructed images of the Derenzo phantom corresponding to the LEHR and the optimized H17 HiSens collimators for the same level of noise in the reconstructed images. When a conventional architecture (1.6 mm pixel size) is associated with the 17 mm thick collimator, the image quality is inferior to that obtained with the LEHR collimator. However, when the HiSens architecture (0.2 mm virtual pixel size) is associated with the H17 collimator, the image features are markedly improved. Comparison of the last three columns of Fig. 17, which correspond to three different collimator-to-detector distances, shows that increasing c has a favorable effect on the high-frequency rod image contrast. The 4.0 mm rods (yellow arrow) are more visible with a 5 mm gap than with a classical 1 mm gap between the collimator and the detector. The contrast of the largest rods is slightly deteriorated due to this increased gap (see dashed arrow and contrast values). We checked that these results remained unchanged when a lower noise level (i.e., a smaller number of iterations) for each method is considered (results not shown).

Considering the DQE curves, the H17 collimator associated with the HiSens architecture and a collimator-to-detector distance of 5 mm was defined as the optimized collimation configuration. Figure 17 shows that the contrast in the 4.0 mm rods observed with the reference collimator is recovered when this optimized collimation configuration is used. Moreover, the smallest rods (1.6 and 2.4 mm), which correspond to the highest frequencies, are slightly better recovered with the optimized H17 HiSens collimator than with the reference LEHR collimator. These results are consistent with the DQE analysis (see Sec. V).

IV.C.2. Derenzo reconstructed images combining several acquisition configurations

Figure 18 shows the image obtained with the adapted OSEM algorithm (see Sec. III D 1), which combines the three HiSens H17 projections ($c=1$, 5, and 10 mm). Only one-third of each projection count number was used for a fair comparison with the reconstructed images corresponding to

Collimator	H29 LEHR Without HiSens processing c = 1 mm	H17 Without HiSens processing c = 1 mm	H17 With HiSens processing c = 1 mm	H17 With HiSens processing c = 5 mm	H17 With HiSens processing c = 10 mm
Iteration number	300 iterations	736 iterations	58 iterations	53 iterations	49 iterations
Reconstructed images		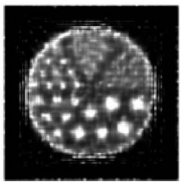	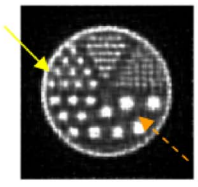	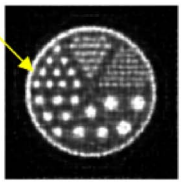	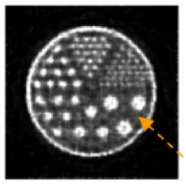
8 mm rod (largest rods) contrast	73.6 %	75.5 %	67.1 %	66.3 %	61.0 %

FIG. 17. Reconstructed images of the Derenzo phantom with the same noise level. Images are shown using common min and max for all images. All GATE-simulated projections used here had the same number of counts (1 Mcount).

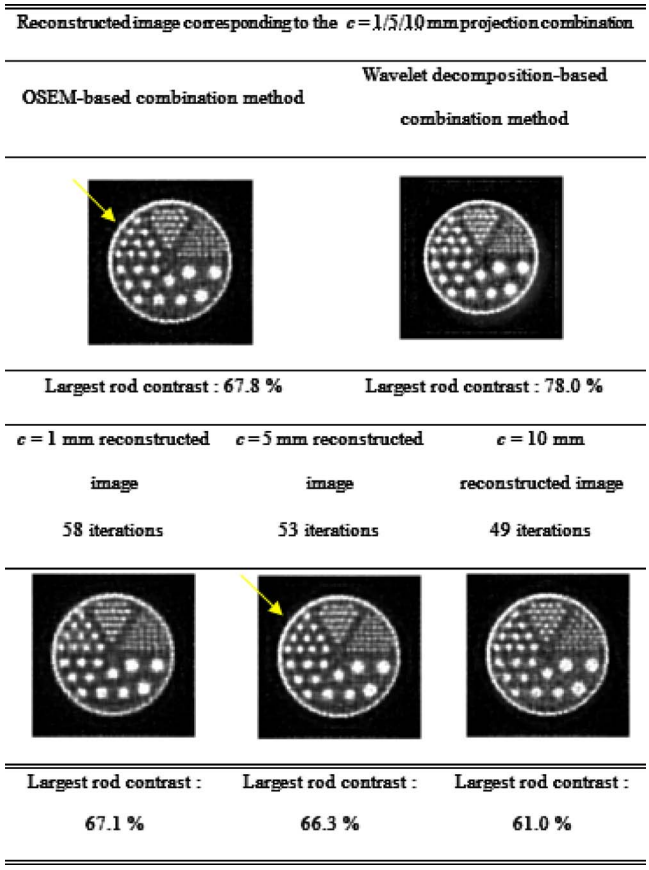

FIG. 18. First row: Images obtained with the optimized H17 HiSens collimator associated with the HiSens architecture, when combining projections acquired with $c=1$, 5, and 10 collimator-to-detector distances (total count number=1 Mcount). Second row: MLEM reconstructed images corresponding to only one collimator-to-detector distance projection.

collimator-to-detector distances of 1, 5, and 10 mm, respectively. When only one collimator-to-detector distance was considered, the OSEM algorithm was actually an MLEM algorithm as only one virtual layer was used. The largest rod (8 mm) contrast is recovered when using the OSEM-based

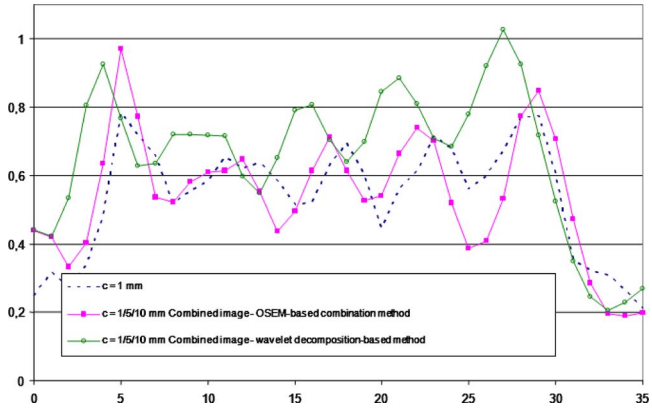

FIG. 19. Profiles through the 2.4 mm rods obtained using the optimized H17 HiSens collimator associated with the HiSens architecture. Solid curve with squares: OSEM-based combination method. Solid curve with circles: Wavelet decomposition-based approach. Dashed curve: Reconstructed image from a single projection corresponding to $c=1$ mm.

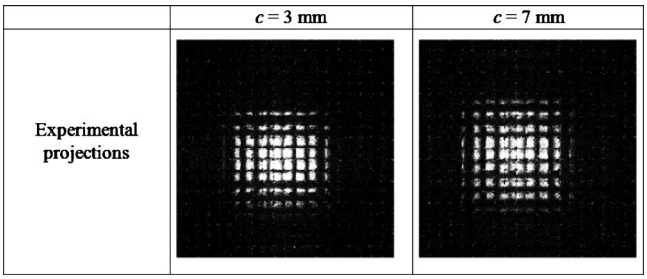

FIG. 20. Experimental projections of the ^{57}Co point source obtained for $c=3$ and $c=7$ mm (0.08 mm virtual pixel size). The H12 high sensitivity collimator was used.

method for combining the three collimator-to-detector projections. The 4 mm rods (yellow arrow) are well recovered in the combined image. The smallest rods (1.6 and 2.4 mm) are slightly better recovered in the combined image than in the $c=1$ mm image (Fig. 19).

Figure 18 also shows the combined image obtained with the wavelet decomposition method. For the largest rods (8, 6.4, and 4.8 mm), the contrast is enhanced using the wavelet decomposition-based method (Fig. 18). However, recovery of the shape of the small rods (4.0, 2.4, and 1.6 mm) is enhanced when the OSEM-based combination algorithm is used.

IV.D. Experimental results

Figure 20 illustrates the experimental projections of the ^{57}Co point source acquired with the H12 high sensitivity collimator for $c=3$ and $c=7$ mm. Virtual pixel size was set to 0.08 mm. As expected, a magnifying pattern can be observed.

Figure 21 shows the experimental DQE curves obtained for $c=3$, 5, and 7 mm when HiSens processing (1 DOI–0.08 mm pixel size) is used. The curves corresponding to a conventional architecture (1 DOI–1.6 mm pixel size) are also plotted for the $c=3$ and 7 mm distances. Without HiSens processing, DQE values corresponding to $c=7$ mm are lower than DQE values obtained for $c=3$ mm. This result confirms that the introduction of a collimator-detector gap is useless without virtual overpixelization. A modulation of the frequencies depending on collimator-to-detector distance can be observed when HiSens processing (1 DOI–0.08 mm pixel size) is used.

V. DISCUSSION

In recent years, CZT detectors have been increasingly studied in medical imaging for their performance and their compact size. When associated with the HiSens architecture, the potential of these detectors is further enhanced.

In this study, we determined the collimator that would make the most of the HiSens architecture for scintimammography applications, using a DQE analysis. Our preliminary results demonstrated that virtual sampling of the CZT detector improved the DQE values and also suggested that the collimator-to-detector distance could play a role in frequency

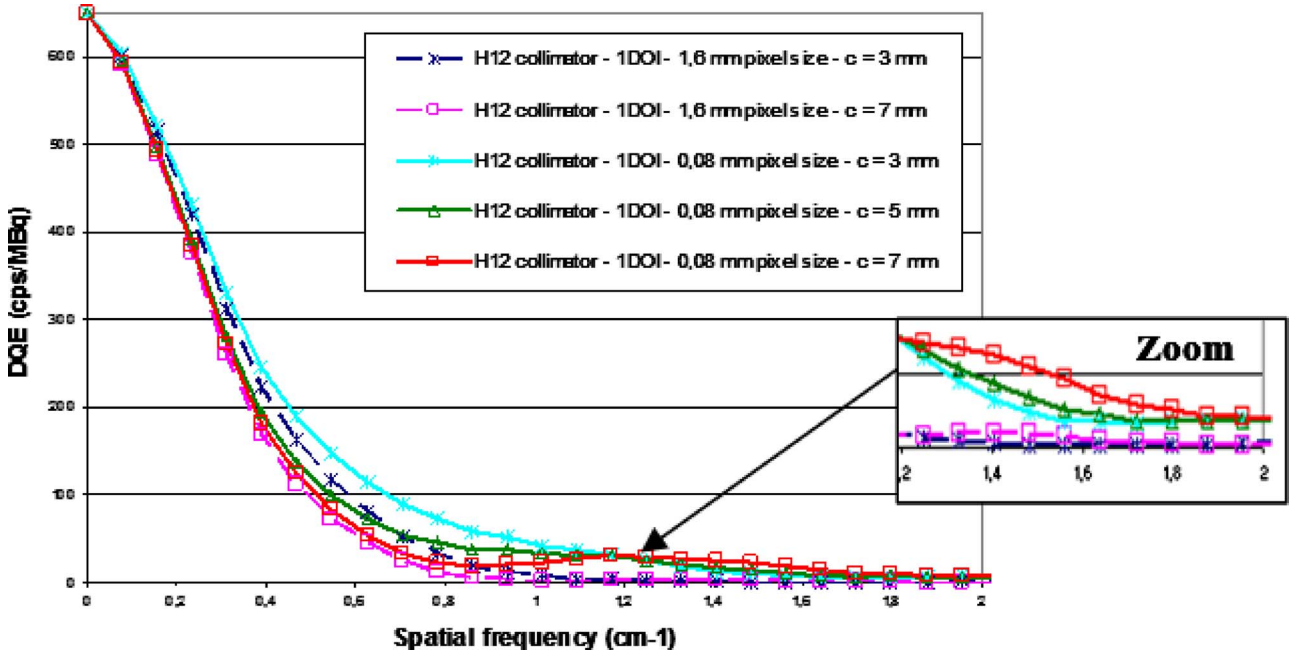

FIG. 21. Experimental DQE values measured for a source-to-collimator distance of 50 mm with the high sensitivity collimator (H12). Two pixel sizes (1.6 and 0.08 mm) and three collimator-to-detector distances (c=3, 5, and 7 mm) were considered.

restoration. This parameter, which cannot be taken advantage of in conventional gamma cameras, is actually useful for modulating DQE curves when the HiSens processing is applied. These simulated results were experimentally validated for a specific setup.

Using the DQE analysis tool and varying the collimator parameters, we found that for a source-collimator distance of 50 mm, the collimator that would recover or even improve the reference LEHR collimator spatial resolution with a maximum gain in sensitivity had a 17 mm septal height and a 1.6 mm pitch, considering a 0.2 mm detector virtual pixel size (64 pixels per collimator hole). A 5 mm gap between the collimator and the detector further improves the high-frequency image content. Images of a Derenzo phantom (Fig. 17) confirm the results of DQE-based optimization and demonstrate the satisfactory match achieved between the DQE curves and the reconstructed images (Fig. 22).

Considering the entire DQE analysis, we showed that a 3.3 increase in sensitivity could be achieved using the HiSens architecture, suggesting that acquisition duration (or injected activity) could be reduced by a factor of 3.3.

We also showed that the collimator-detector gap could impact the DQE curves. This feature could be taken advantage of using at least three strategies:

(1) The object frequency content is unknown—A c distance, which smoothes the DQE curve and thus prevents both low- and high-frequency hollows, can be determined for each collimation geometry. In the H17 collimation case studied, c is about 5 mm.
(2) The frequencies of interest for the considered object are known *a priori* (using a prescan or a scout image)—A c distance that maximizes the DQE values for the frequencies of interest can be determined and used for imaging.
(3) Several acquisitions corresponding to different c distances can be performed and combined.

Our results could be taken advantage of for the adaptive SPECT imaging concept recently developed,[38–41] in which two-step protocols are encouraged. In our case, a quick scout image could be performed to roughly identify the characteristic frequencies of the object of interest. The best collimation configuration could then be selected based on the previously tabulated DQE curves. Equipment should obviously be available to accurately tune the collimator-to-detector distance.

To make the most of images acquired for different collimator-to-detector distances, two projection combination methods have been proposed (Sec. III D). The corresponding results suggest that there might be an advantage in operating at several collimator-to-detector distances to better recover the frequency content of the object of interest. This will, however, require further investigation.

The main aim of the work was to study the effects of fine 3D spatial sampling on image quality, collimation optimization, and associated efficiency gain. An ideal detector was thus considered (no modeling of the intrinsic spatial resolution). Preliminary experimental studies suggest that a 400 μm intrinsic spatial resolution can be obtained with barycentric positioning. This will be included in future simulations of the detector. In this work, a CZT detector was considered. The method could, however, be extended to other materials such as scintillators if small physical or virtual pixel sizes become achievable.

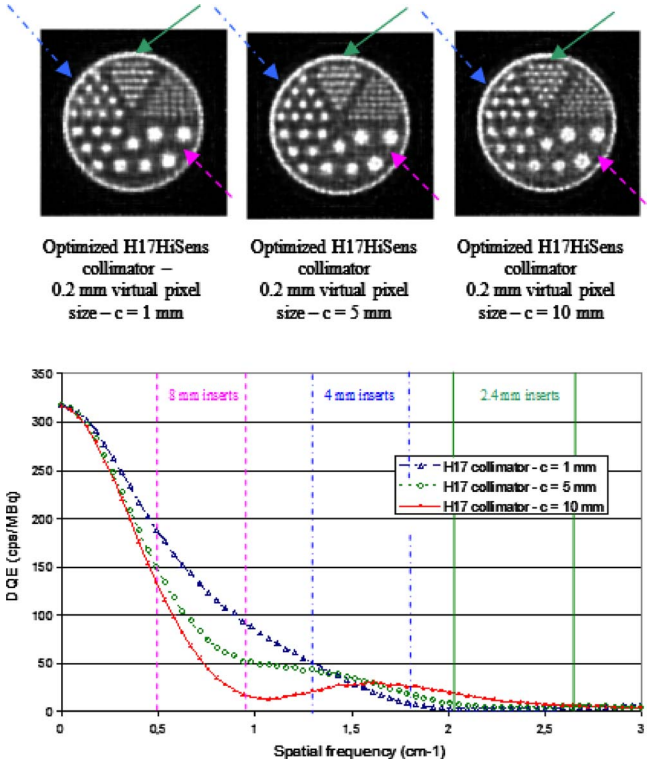

FIG. 22. DQE measured for a 50 mm source-to-collimator distance for the optimized H17 HiSens collimator. In each configuration, HiSens processing was used (3 DOI–0.2 mm virtual pixel size). *c* was set to 1, 5, and 10 mm. Positions of the Derenzo rods of interest are shown to explain the resolution recovery observed in the reconstructed images.

VI. CONCLUSION

In this study dedicated to scintimammography applications, the relevance of the HiSens architecture was demonstrated. DQE computations and Monte Carlo simulations both showed that accurate 3D positioning of interactions in the CZT detector associated with an appropriate collimator-detector gap made it possible to increase detection sensitivity while maintaining or improving the spatial resolution of a reference LEHR collimator. Considering a 50 mm source-collimator distance, we showed that an increase in sensitivity by a factor of 3.3 could be achieved, suggesting that acquisition duration or injected activity could be markedly reduced if this HiSens architecture was used. Processing approaches to make the most of the acquired data were also presented and showed that combining data acquired with different collimator-detector gaps could further improve restoration of the frequency content of the images.

[a]Electronic mail: guillaume.montemont@cea.fr

[1]S. Parker, T. Tong, S. Bolden, and P. A. Wingo, "Cancer statistics," Ca-Cancer J. Clin. **47**, 5–27 (1997).
[2]T. J. Rissanen, H. P. Mäkäräinen, S. I. Mattila, and E. L. Lindholm, "Breast cancer recurrence after mastectomy: Diagnosis with mammography and US," Radiology **188**, 463–467 (1993).
[3]L. L. Humphrey, M. Helfand, B. K. S. Chan, and S. H. Woolf, "Breast cancer screening: A summary of the evidence for the U.S. Preventive Services Task Force," Ann. Intern Med. **137**, 347–360 (2002).
[4]P. A. Carney *et al.*, "Individual and combined effects of age, breast density, and hormone replacement therapy use on the accuracy of screening mammography," Ann. Intern Med. **138**, 168–175 (2003).
[5]I. Laconte *et al.*, "Mammography and subsequent whole-breast sonography of nonpalpable breast cancers: The importance of radiologic breast density," AJR, Am. J. Roentgenol. **180**, 1675–1679 (2003).
[6]T. M. Kolb, J. Lichy, and J. H. Newhouse, "Comparison of the performance of screening mammography, physical examination, and breast ultra-sound and evaluation of factors that influence them: An analysis of 27,825 patient evaluations," Radiology **225**, 165–175 (2002).
[7]N. F. Boyd *et al.*, "Mammographic density and the risk and detection of breast cancer," N. Engl. J. Med. **356**, 227–236 (2007).
[8]L. Pan, Y. Han, X. Sun, J. Liu, and H. Gang, "FDG-PET and other imaging modalities for the evaluation of breast cancer recurrence and metastases: A meta-analysis," J. Cancer Res. Clin. Oncol. **136**, 1007–1022 (2010).
[9]C. L. Maini *et al.*, "$^{99\text{-}m}$Tc-MIBI scintimammography using a dedicated nuclear mammograph," J. Nucl. Med. **40**, 46–51 (1999).
[10]L. R. Coover, G. Caravaglia, and P. Kuhn, "Scintimammography with dedicated breast camera detects and localizes occult carcinoma," J. Nucl. Med. **45**, 553–558 (2004).
[11]C. B. Hruska, M. K. O'Connor, and D. A. Collins, "Comparison of small field of view gamma-camera systems for scintimammography," Nucl. Med. Commun. **26**, 441–445 (2005).
[12]C. B. Hruska and M. K. O'Connor, "CZT detectors: How important is energy resolution for nuclear breast imaging?," Phys. Med. **21**, 72–75 (2006).
[13]R. F. Brem, A. C. Floerke, J. A. Rapelyea, C. Teal, T. Kelly, and V. Mathur, "Breast-specific gamma imaging as an adjunct imaging modality for the diagnosis of breast cancer," Radiology **247**, 651–657 (2008).
[14]R. F. Brem, M. Loffe, J. A. Rapelyea, K. G. Yost, J. M. Weigert, M. L. Bertrand, and L. H. Stern, "Invasive lobular carcinoma: Detection with mammography, sonography, MRI, and breast-specific gamma imaging," AJR, Am. J. Roentgenol. **192**, 379–383 (2009).
[15]E. A. Jones, T. D. Phan, D. A. Blanchard, and A. Miley, "Breast-specific gamma-imaging: Molecular imaging of the breast using $^{99\ m}$Tc-sestamibi and a small field of view gamma-camera," J. Nucl. Med. Technol. **37**, 201–205 (2009).
[16]A. L. Weinmann, C. B. Hruska, and M. K. O'Connor, "Design of optimal collimation for dedicated molecular breast imaging systems," Med. Phys. **36**, 845–856 (2009).
[17]D. J. Rhodes M. K. O'Connor, S. W. Phillips R. L. Smith, and D. A. Collins, "Molecular breast imaging: A new technique using technetium Tc 99m scintimammography to detect small breast tumours of the breast," Mayo Clin. Proc. **80**, 24–30 (2005).
[18]M. K. O'Connor, S. W. Phillips, C. B. Hruska, D. J. Rhodes, and D. A. Collins, "Molecular breast imaging: Advantages and limitations of a scintimammographic technique in patients with small breast tumours," Breast J. **13**, 3–11 (2007).
[19]I. M. Blevis, M. K. O'Connor, Z. Keidar, A. Pansky, H. Altman, and J. W. Hugg, "CZT gamma camera for scintimammography," Phys. Med. **21**, 56–59 (2006).
[20]B. Mueller *et al.*, "Evaluation of small CET detector for scintimammography," J. Nucl. Med. **44**, 602–609 (2003).
[21]L. Verger, M. C. Gentet, R. Guillemaud, C. Mestais, O. Monnet, G. Montémont, G. Petroz, J. P. Rostaing, and J. Rustique, "Performance and perspectives of a CdZnTe based gamma camera for medical imaging," IEEE Trans. Nucl. Sci. **51**, 3111–3117 (2004).
[22]International Commission on Radiological Protection, "Radiation dose to patients from radiopharmaceuticals: Publication 80," Ann. ICRP **28**, 85–111 (1998).
[23]L. Guerin, L. Verger, V. Rebuffel, and O. Monnet, "A new architecture for pixelated solid state gamma camera used in nuclear medicine," IEEE Trans. Nucl. Sci. **55**, 1573–1580 (2008).
[24]E. Gros d'Aillon, M. C. Gentet, G. Montemont, J. Rustique, and L. Verger, "Simulation and experimental results on monolithic CdZnTe gamma-ray detectors," IEEE Trans. Nucl. Sci. **52**, 3096–3102 (2005).
[25]G. Montemont, T. Bordy, V. Rebuffel, C. Robert, and L. Verger, "CZT pixel detectors for improved SPECT imaging," IEEE RTSD Conference Record, pp. 84–89, 2008 (unpublished).
[26]C. Robert, G. Montemont, V. Rebuffel, I. Buvat, L. Guérin, and L. Verger, "Simulation-based evaluation and optimization of a new CdZnTe gamma-camera architecture (HiSens)," Phys. Med. Biol. **55**, 2709–2726 (2010).
[27]W. K. Warburton, "An approach to sub-pixel spatial resolution in room temperature x-ray detector arrays with good energy resolution," Semiconductors for Room-Temperature Radiation Detector Applications II: Mate-

rials Research Society Symposium Proceeding, 1997 (unpublished).
[28]S. E. Anderson, B. Dönmez, and Z. He, "Sub-pixel position resolution in pixelated semiconductor detectors," IEEE NSS Conference Record, Vol. 2, pp. 1569–1576, 2007 (unpublished).
[29]J. Kim, B. Dönmez, K. Nelson, and Z. He, "Three-dimensional signal correction on UltraPeRL CZT detectors," IEEE NSS Conference Record, Vol. 2, pp. 1289–1293, 2007 (unpublished).
[30]S. Starck, M. Bath, and S. Carlsson, "The use of detective quantum efficiency (DQE) in evaluating the performances of gamma cameras systems," Phys. Med. Biol. **50**, 1601–1609 (2005).
[31]J. Tabary, R. Guillemaud, and F. Mathy, "Combination of high resolution analytically computed uncollided flux images with low resolution Monte Carlo computed scattered flux images," IEEE Trans. Nucl. Sci. **51**, 212–217 (2004).
[32]I. Khalkhali, L. E. Diggles, T. Taillefer, P. R. Vandesstreek, P. J. Peller, and H. H. Abdel-Nabi, "Procedure guidelines for breast scintigraphy," J. Nucl. Med. **40**, 1233–1235 (1999).
[33]C. B. Hruska and M. K. O'Connor, "Effect of collimator selection on tumor detection for dedicated nuclear breast imaging systems," IEEE Trans. Nucl. Sci. **53**, 2680–2689 (2006).
[34]S. Jan *et al.*, "GATE: A simulation toolkit for PET and SPECT," Phys. Med. Biol. **49**, 4543–4561 (2004).
[35]J. Maublant, "Technetium-99m-sestamibi uptake in breast tumor and associated lymph nodes," J. Nucl. Med. **37**, 922–925 (1996).
[36]S. G. Mallat, "A theory for multiresolution signal decomposition: The wavelet representation," IEEE Trans. Pattern Anal. Mach. Intell. **11**, 674–693 (1989).
[37]S. Mallat and S. Zhong, "Characterization of signals from multiscale edges," IEEE Trans. Pattern Anal. Mach. Intell. **14**, 710–732 (1992).
[38]H. Barrett, L. R. Furenlid, M. Freed, J. Y. Hesterman, M. A. Kupinski, E. Clarkson, and M. K. Whitaker, "Adaptive SPECT," IEEE Trans. Med. Imaging **27**, 775–788 (2008).
[39]L. Caucci, M. A. Kupinski, M. Freed, L. R. Furenlid, D. W. Wilson, and H. Barrett, "Adaptive SPECT for tumor necrosis detection," IEEE Trans. Nuclear Science Conference Record, Vol. 27, pp. 5548–5551, 2008 (unpublished).
[40]J. W. Moore, L. R. Furenlid, and H. H. Barrett, "Instrumentation design for adaptive SPECT/CT," IEEE Nuclear Science Symposium Conference Record, pp. 5585–5587, 2008 (unpublished).
[41]L. R. Furenlid, J. W. Moore, M. Freed, M. A. Kupinski, E. Clarkson, Z. Liu, D. W. Wilson, J. M. Woolfender, and H. H. Barrett, "Adaptive small-animal SPECT-CT," Biomedical Imaging: From Nano to Macro (ISBI), pp. 1407–1410, 2008 (unpublished).